JVST A
Journal of Vacuum Science & Technology A
ARTICLE
pubs.aip.org/avs/jva

Thermal atomic layer etching of SnO_2 by fluorination and ligand-exchange/conversion reactions using sequential hydrogen fluoride and $Al(CH_3)_3$ exposures

Cite as: J. Vac. Sci. Technol. A **44**, 022604 (2026); doi: 10.1116/6.0005016
Submitted: 30 September 2025 · Accepted: 12 December 2025 ·
Published Online: 14 January 2026

View Online Export Citation CrossMark

Chen Li,[1] Jonathan L. Partridge,[1] Troy A. Colleran,[1] Micah H. Duffield,[1] Yong Hyun Ham,[2] and Steven M. George[1]

AFFILIATIONS

[1] Department of Chemistry, University of Colorado, Boulder, Colorado 80309
[2] Etch Team, SEMES, Hyohaeng-ro, Hwaseong-si, Gyeonggi-do, Republic of Korea

Note: This paper is part of the Special Topic on Atomic Layer Etching (ALE).

ABSTRACT

Thermal atomic layer etching (ALE) of SnO_2 was performed using a sequence of self-limiting fluorination and subsequent ligand-exchange/conversion reactions. The trimethylaluminum (TMA) can convert the SnO_2 surface to an Al_2O_3 layer. Hydrogen fluoride (HF) then fluorinates the Al_2O_3 surface layer to form metal fluoride. Subsequently, TMA undergoes a ligand-exchange reaction and removes the metal fluoride by forming volatile products before again converting SnO_2 to Al_2O_3. The initial SnO_2 layers were prepared via atomic layer deposition by employing tetrakis(dimethylamino) tin and H_2O_2. The thermal SnO_2 ALE was then studied using various techniques, including quartz crystal microbalance (QCM), x-ray reflectivity (XRR), quadrupole mass spectrometry (QMS), and atomic force microscopy (AFM) measurements. *In situ* QCM experiments monitored SnO_2 ALE at temperatures from 225 to 300 °C. A linear reduction in SnO_2 mass was observed as the number of HF and TMA cycles increased. QCM measurements confirmed that both HF and TMA reaction steps reached saturation with respect to reactant exposures, indicating self-limiting behavior. Higher etching temperatures led to higher SnO_2 removal rates. The QCM analysis measured mass change per cycle (MCPC) values that varied from −32.6, −44.2, −100.2, and−123.5 ng/(cm^2 cycle) at 225, 250, 275, and 300 °C, respectively. These MCPCs correspond to SnO_2 etch rates of 0.47, 0.64, 1.44, and 1.78 Å/cycle for 225, 250, 275, and 300 °C, respectively. XRR measurements confirmed the linear removal of the SnO_2 film thickness and the etching rates. QMS analysis also revealed the volatile etching products during the sequential HF and TMA exposures on SnO_2 at 300 °C. These QMS investigations monitored $Sn(CH_3)_3^+$ ion intensities during TMA exposures. The $Sn(CH_3)_3^+$ ion intensity was consistent with $Sn(CH_3)_4$ as the main Sn etch product. In addition, $Al_xF_y(CH_3)_z$ dimer and trimer species were identified as the ligand-exchange products. QMS studies also revealed that $Al(CH_3)_3$ exposures on initial SnO_2 substrates prior to fluorination released $Sn(CH_3)_4$ products. These $Sn(CH_3)_4$ products are expected if $Al(CH_3)_3$ can convert SnO_2 to Al_2O_3. These results indicate that $Al(CH_3)_3$ can both convert the SnO_2 surface to an Al_2O_3 layer and remove the fluorinated Al_2O_3 layer by ligand-exchange reactions. The conversion and ligand-exchange reactions both produce $Sn(CH_3)_4$. Atomic force microscopy measurements also indicated that multiple thermal ALE cycles did not significantly change the roughness of the SnO_2 surface.

I. INTRODUCTION

Transparent conductive oxides have emerged as a pivotal class of materials in modern electronics due to their unique combination of optical transparency and electrical conductivity.[1,2] Among these, tin dioxide (SnO_2) stands out as a highly versatile and widely utilized material, owing to its excellent thermal stability, wide bandgap, and superior electron mobility.[3,4] These properties make SnO_2 indispensable in a variety of applications, including flat panel displays and photovoltaic devices, solar cells, gas sensors, and thin-film transistors.[5,6]

In recent years, the development of SnO_2-based devices has gained significant attention. Advanced fabrication techniques, such as atomic layer deposition (ALD), have enabled the precise growth of SnO_2 thin films with excellent uniformity and conformality, making them feasible for integration into nano-electronic devices. For example, SnO_2 ALD films have been used to fabricate channels for high-performance back-end-of-line compatible field effect transistors.[7,8] SnO_2 ALD thin films have also been successfully utilized as electron transport layers in perovskite solar cells, significantly advancing their performance and stability.[9,10] Additionally, SnO_2 ALD-based gas sensors have demonstrated high sensitivity to gases like H_2, O_3, CO, and NO_2, making them valuable for environmental monitoring.[11,12]

Precise etching of SnO_2 is necessary and critical for many applications. For example, tuning the thickness of the SnO_2 channels in field effect transistors optimizes their performance.[7] Controlling the thickness of tin oxide gas sensor films also enhances their sensing performance.[11] Unfortunately, there have not been many reported methods for etching SnO_2 thin films. Wet chemical etching methods have utilized aqueous solutions of HI or HCl acids.[13,14] Wet etching does not produce anisotropic etching and has difficulty achieving fine patterning because of pattern collapse.[15] Dry etch processes have employed chlorine, fluorine, or bromine-based plasmas.[16,17] While these plasma etching methods have been successfully employed, they also have negative consequences. One difficulty is that ion bombardment during plasma etching can lead to surface damage.[18]

In contrast, thermal atomic layer etching (ALE) offers a promising alternative removal method that enables precise control at the atomic layer level.[19,20] Thermal ALE is based on gas phase, sequential, and self-limiting surface reactions that can be viewed as the opposite of the ALD process.[20,21] The first thermal reaction modifies the top layer of the material surface. The second thermal reaction then leads to the volatilization of the modified surface layer.[20] Thermal ALE enables isotropic etching because gaseous reactants can uniformly access the entire surface area of three-dimensional and high-aspect-ratio structures.[19,22,23]

Many mechanisms for thermal ALE have developed in recent years.[20] For metal oxides and nitrides, fluorination is commonly employed as the surface modification step, followed by ligand-exchange reactions to transform the modified surface layer into volatile species.[20,24] This approach has proven highly effective for materials such as Al_2O_3, HfO_2, ZrO_2, Ga_2O_3, GaN, and AlN.[22,25–31]

In addition, conversion has emerged as an important mechanism in thermal etching reactions. For materials like SiO_2, ZnO, VO_2, and Al_2O_3,[32–35] precursors can be used to convert the initial surface material into another material that facilitates the etching process. For certain semiconductor materials, such as Si, SiGe, and Si_3N_4, thermal etching can be achieved using strategies that combine oxidation, conversion, fluorination, and ligand-exchange reactions.[36–38] The thermal etching of elemental metals has also been developed for metals such as Ni, Cu, and Co. Surface modification can be achieved through oxidation or chlorination, followed by the volatilization of surface species by ligand addition or ligand substitution reactions.[39–41]

In this work, a thermal ALE process for SnO_2 was demonstrated using sequential self-limiting ligand-exchange/conversion and fluorination reactions as illustrated in Fig. 1. Trimethylaluminum (TMA) was employed as the ligand-exchange/conversion reactant. The fluorination step utilized hydrogen fluoride (HF) as the reactant.

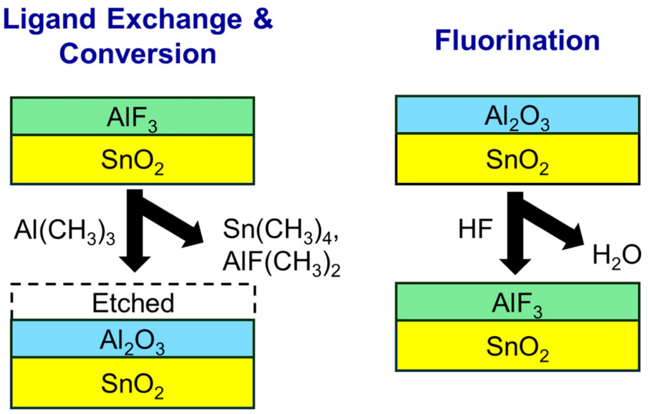

FIG. 1. Proposed mechanism for SnO_2 ALE using HF for fluorination and TMA for ligand exchange and conversion.

The etch rate of SnO_2 ALE was characterized by *in situ* quartz crystal microbalance (QCM) and *ex situ* x-ray reflectivity (XRR). The volatile products released during each reactant exposure were detected and identified using quadrupole mass spectrometry (QMS) analysis. The surface morphology before and after ALE cycles was also measured by atomic force microscopy (AFM) to determine the effect of thermal ALE on surface roughness.

II. EXPERIMENTAL SECTION

A. Viscous flow reactor with *in situ* QCM

SnO_2 ALD and the subsequent SnO_2 thermal ALE experiments were performed in a hot-wall viscous flow reactor.[42] The reactor temperature was controlled by a proportional-integral-derivative temperature controller (2604, Eurotherm), together with a power controller (Epack, Eurotherm). These controllers regulated the reactor temperature with a precision of ±0.1 °C. A mechanical rotary vane pump (2010C1, Pfeiffer) was attached to the back of the reactor. The base reactor pressure was 1 Torr with a constant flow at 150 SCCM of ultrahigh-purity (UHP) Ar gas (99.999%, Airgas). This pressure was measured using a capacitance manometer (Baratron 121A, MKS).

The mass change of the SnO_2 films during the ALD and thermal ALE processes was monitored by an *in situ* QCM.[42] The QCM sensor was a quartz crystal [gold-coated and polished, radiation compensated cut, 6 MHz, Phillip Technologies] placed in a bakable single sensor head (BSH-150, Inficon) and sealed with a high-temperature silver epoxy (Epo-Tek H21D, Epoxy Technology Inc.). The QCM head was positioned in the isothermal region of the reactor. The QCM was placed in the reactor at experimental temperature for at least 5 h to equilibrate before starting experiments.

To prevent any deposition or etching on the backside of the QCM crystal, an additional constant Ar gas flow at 30 SCCM traveled through the QCM housing. The changes in resonant frequency of the quartz crystal were recorded and converted to mass using a thin-film deposition monitor (Maxtek TM-400, Inficon) during the ALD and thermal ALE processes. The QCM has a precision of ~0.4 ng/cm^2.

To start each ALE study, *in situ* QCM crystal was first coated with a freshly deposited SnO_2 film grown by ALD. Initially, 50 cycles of TMA (97%, Sigma-Aldrich) and H_2O were used as the reactants to grow an Al_2O_3 ALD layer to help the subsequent nucleation of the SnO_2 ALD film. Both TMA and H_2O reactants were kept at ambient temperature during the process. Subsequently, the SnO_2 ALD layer was deposited using tetrakis(dimethylamino) tin (TDMASn, Gelest, >95% purity) and hydrogen peroxide (H_2O_2, Aldrich, 50 wt. % in water). The SnO_2 ALD growth rate at 150 °C was 0.98 Å/cycle in agreement with earlier results.[43]

The thermal SnO_2 ALE experiments used TMA (97%, Sigma-Aldrich) as the ligand-exchange/conversion precursor. HF-pyridine (70 wt. % HF, Sigma-Aldrich) was employed as the source of the HF reactant. Pressure transients for TMA were ~40 mTorr at room temperature. Pressure transients for HF were ~90 mTorr at room temperature. The TMA and HF pressure transients were both controlled by metering valves (SS-4BMG, Swagelok).

B. ALD and ALE on silicon wafers for *ex situ* film analysis

SnO_2 ALD films used in the SnO_2 ALE experiments were deposited on boron-doped Si wafers [p type, (100), Silicon Valley Microelectronics]. The wafers were diced into 2×2 cm^2 pieces and cleaned sequentially with acetone, isopropanol, and de-ionized water to remove surface contaminants. After drying the substrates with UHP nitrogen, they were placed in the reactor and allowed at least 2 h to reach thermal equilibrium. The SnO_2 ALD and SnO_2 ALE were performed on these Si wafers for *ex situ* film analysis.

Grazing incidence x-ray diffraction was used to characterize the crystallinity of the SnO_2 film. The density and thickness of the SnO_2 films were measured by XRR. The comparison of the SnO_2 thickness before and after the ALE process determined the etch rate. Both x-ray diffraction (XRD) and XRR scans were accomplished using an x-ray diffractometer (Bede D1, Jordan Valley Semiconductors). The measurements were carried out using Cu K_α radiation ($\lambda = 1.54$ Å). The x-ray tube operated at 40 kV and 35 mA. For the XRD scans, the incident x-ray angle was set to 0.3°. XRR data were collected over a range of 300–6000 arc sec with a step size of 5 arc sec. The XRD patterns were processed using JORDAN VALLEY POLYCRYSTAL software (Jordan Valley Semiconductors), and the XRR data were modeled and fitted with BEDE REFS software (Jordan Valley Semiconductors).

AFM measurements were performed to characterize changes in the surface roughness of SnO_2 films before and after thermal ALE processes. A Park NX-10 AFM instrument was used to perform the AFM measurements using the noncontact mode. The scan rate was 0.8 Hz using an Olympus microcantilever probe (OMCL-AC160TS). XEI software (Park system) was utilized to analyze the parameters of the AFM images.

C. QMS investigations to identify volatile etch products

QMS studies of SnO_2 ALE were conducted to identify the volatile etch products. The experiments were performed in a custom-designed reactor using high-surface-area powders for enhanced sensitivity.[44] High-purity crystalline SnO_2 nanopowders with diameters from 35 to 55 nm (US Research Nanomaterials Inc.) were loaded into the sample holder. The precursors were introduced through separate inlet lines that terminated before the sample holder.[44]

The precursors were alternately exposed to the SnO_2 powder. The etch products were transported out of the sample holder by the N_2 carrier gas. A portion of the gas stream passed through an aperture into a low-pressure differentially-pumped region and formed a molecular beam.[45] This molecular beam was intercepted by a skimmer that allowed the center of the beam to pass to the QMS ionizer.[45] The etch products were analyzed using a quadrupole mass spectrometer (Extrel, MAX-QMS flange-mounted system).

III. RESULTS AND DISCUSSION

A. Initial SnO_2 ALD films

The initial SnO_2 ALD films were first grown on the QCM sensor surface. Figure 2 shows the growth of the SnO_2 ALD films at 150 °C using 50 cycles of sequential TDMASn and H_2O_2 exposures. The reaction time sequence was 1 s–10 s–1 s–10 s. 1 s was used for both TDMASn and H_2O_2 exposure times. Ten seconds was the Ar purging time after the precursor dosing. The SnO_2 ALD growth was linear versus the number of ALD cycles and yielded a mass gain per cycle (MGPC) of 68.11 ng/(cm^2 cycle). This MGPC is equivalent to a growth rate of 0.98 Å/cycle based on the SnO_2 film density of 6.95 g/cm^3. This result agrees with the previous SnO_2 ALD study using TDMASn and H_2O_2 where the growth rate was 0.96 Å/cycle at 150 °C.[43]

The SnO_2 ALD films initially prepared on the silicon wafers were examined by XRD. Figure 3(a) displays the diffraction pattern for a SnO_2 layer produced on a Si (100) wafer using 500 TDMASn and H_2O_2 ALD cycles at 200 °C. This SnO_2 ALD film had a thickness of ~50 nm. The XRD peaks are consistent with polycrystalline SnO_2. The tetragonal rutile crystalline structure of SnO_2 (JCPDS

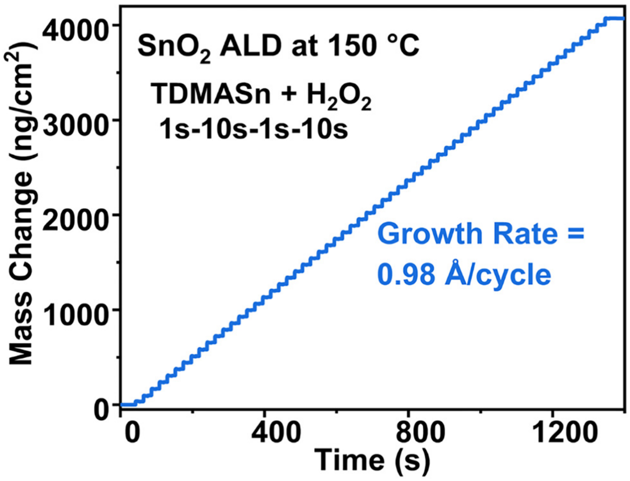

FIG. 2. Mass changes vs time during 60 SnO_2 ALD cycles using TDMASn and H_2O_2 with a 1 s–10 s–1 s–10 s reaction sequence at 150 °C.

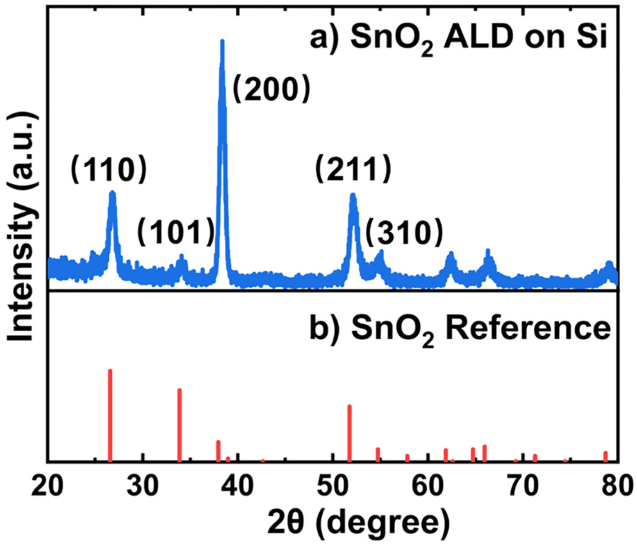

FIG. 3. (a) Grazing incidence XRD spectrum for the SnO_2 substrate grown using 500 cycles of SnO_2 ALD on a Si (100) wafer at 200 °C. (b) Reference for the SnO_2 tetragonal rutile crystalline structure.

No. 41-1445) is shown in Fig. 3(b). There is good agreement between the diffraction peaks in Fig. 3(a) and the assignments for the tetragonal rutile crystalline structure in Fig. 3(b).

B. SnO_2 ALE using QCM investigations

The SnO_2 ALD films were utilized for the SnO_2 thermal ALE experiments. Figure 4 shows the QCM mass evolution over time during 50 ALE cycles consisting of alternating HF and TMA exposures, respectively. The SnO_2 ALD and ALE were both performed at 300 °C. Each ALE cycle consisted of a 2 s HF dose, a 30 s Ar purge, a 2 s TMA dose, and a second 30 s Ar purge, corresponding to a 2 s–30 s–2 s–30 s sequence. During SnO_2 ALE, the HF and TMA pulses generated pressure transients of approximately 100 and 40 mTorr, respectively.

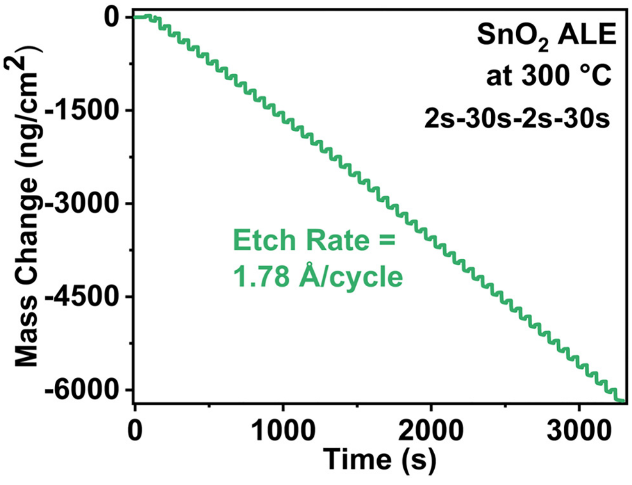

FIG. 4. QCM mass change vs time for SnO_2 ALE using 50 sequential HF and TMA exposures at 300 °C with a 2 s–30 s–2 s–30 s reaction sequence.

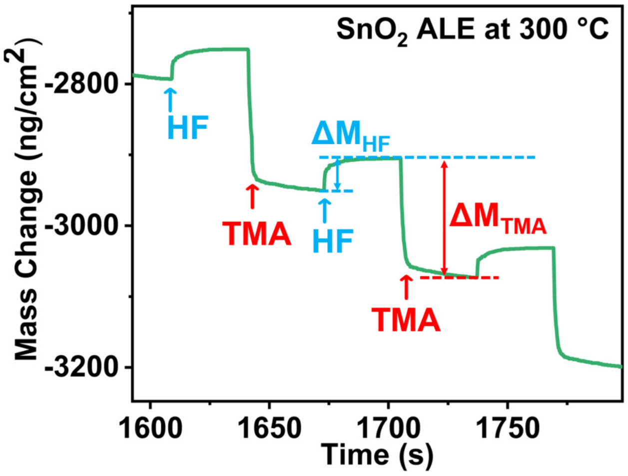

FIG. 5. Expansion of three cycles in Fig. 4 showing mass changes during SnO_2 ALE using sequential HF and TMA exposures at 300 °C.

Figure 4 shows a linear mass loss versus the number of HF and TMA exposures during SnO_2 ALE. This constant mass loss for every HF and TMA cycle yields a mass change per cycle (MCPC) of -123.5 ng/(cm^2 cycle). This MCPC corresponds to an etch per cycle of 1.78 Å/cycle. The etch rate was determined using the equality 1 Å $SnO_2/cm^2 = 69.5$ ng SnO_2/cm^2 based on a SnO_2 density of 6.95 g/cm^3.

Figure 5 shows an expansion of the QCM results during three sequential cycles of HF and TMA exposures during SnO_2 ALE at 300 °C. These results can be examined to understand the mechanism of thermal SnO_2 ALE. Figure 5 clearly shows that the mass increases during each HF exposure. The mass increase for each HF exposure at 300 °C is $\Delta M_{HF} = +40.6$ ng/cm^2. This mass gain is expected from the fluorination reaction.

The fluorination reaction could be the fluorination of SnO_2,

$$SnO_2 + 4HF(g) \rightarrow SnF_4 + 2H_2O(g). \qquad (1)$$

However, this reaction is not thermochemically favorable. The standard Gibbs free energy change for the reaction in Eq. (1) is ΔG° (300 °C) = +32.8 kcal.[46] Because SnO_2 fluorination by HF is not predicted to be spontaneous, the mass gain during the HF exposure is believed to result from Al_2O_3 fluorination as shown in Fig. 1. A thin Al_2O_3 layer is on the SnO_2 surface as a result of the conversion of SnO_2 to Al_2O_3 as illustrated in Fig. 1. This conversion reaction is supported by the QMS studies that are described later. The fluorination reaction of Al_2O_3 by HF is given by

$$Al_2O_3 + 6HF(g) \rightarrow 2AlF_3 + 3H_2O(g). \qquad (2)$$

This reaction is thermochemically favorable with a standard Gibbs free energy change of $\Delta G°$ (300 °C) = −49.1 kcal.[46]

The mass increase of $\Delta M_{HF} = +40.6$ ng/cm^2 can be employed to estimate the thickness of the AlF_3 layer after the HF exposure. The mass change in atomic mass units for the reaction in Eq. (2) is +66.0 amu or 1.096×10^{-22} g. The mass change of $\Delta M_{HF} = +40.6$ ng/cm^2 divided by 1.096×10^{-22} g yields 7.41×10^{14} AlF_3 units/cm^2 produced during the fluorination reaction. This coverage of AlF_3 units/cm^2 is equivalent to 103.35 ng of AlF_3/cm^2. This mass of AlF_3/cm^2 divided by the AlF_3 density of 2.88 g/cm^3 yields an AlF_3 thickness of 3.58×10^{-8} cm.

Figure 5 also reveals mass decreases during each TMA exposure. The mass decrease is consistent with the removal of the AlF_3 layer by ligand exchange with TMA according to:

$$2AlF_3 + 4Al(CH_3)_3(g) \rightarrow 6AlF(CH_3)_2(g). \tag{3}$$

The TMA can then proceed to convert the underlying SnO_2 to Al_2O_3. This reaction can be written as

$$1.5SnO_2 + 2Al(CH_3)_3(g) \rightarrow Al_2O_3 + 1.5Sn(CH_3)_4(g). \tag{4}$$

The mass decrease for each TMA exposure is $\Delta M_{TMA} = -164.7$ ng/cm^2. The removal of the AlF_3 layer would lead to a mass loss of 103.35 ng/cm^2. The remaining mass loss of 61.35 ng/cm^2 can then be attributed to the conversion of SnO_2 to Al_2O_3.

This mass loss of 61.35 ng/cm^2 can be used to determine the Al_2O_3 thickness produced by TMA conversion of SnO_2. The mass loss in atomic mass units for the reaction in Eq. (4) is 124.10 amu or 2.06×10^{-22} g. The mass loss of 61.35 ng/cm^2 divided by the mass loss of 2.06×10^{-22} g for the reaction in Eq. (4) yields 2.98×10^{14} Al_2O_3 units/cm^2 produced during the conversion reaction. This coverage of Al_2O_3 units/cm^2 is equivalent to 5.04×10^{-8} g of Al_2O_3/cm^2. This mass of Al_2O_3/cm^2 divided by the Al_2O_3 density of 3.9 g/cm^3 yields an Al_2O_3 thickness of 1.29×10^{-8} cm.

Figure 6 shows ΔM_{TMA}, ΔM_{HF}, and the MCPC versus the number of ALE cycles at 300 °C. MCPC is defined as MCPC = $\Delta M_{HF} + \Delta M_{TMA}$. Across the 50 ALE cycles, ΔM_{HF}, ΔM_{TMA}, and MCPC remain essentially constant at +40.6, −164.7, and −124.0 ng/cm^2, respectively. The mass shifts during the initial few SnO_2 ALE cycles differ from those observed in the later cycles. These variations are believed to arise from the initiation of the SnO_2 ALE process.

C. Dependence of SnO_2 ALE on reaction parameters

The self-limiting nature of the HF and TMA reactions during SnO_2 ALE is examined at 275 °C in Fig. 7. The MCPC for SnO_2

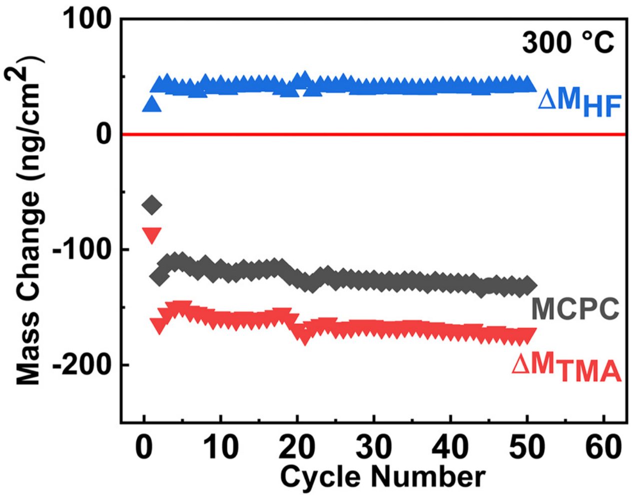

FIG. 6. Mass changes during individual HF exposures (ΔM_{HF}), TMA exposures (ΔM_{TMA}), and the total MCPC for SnO_2 ALE at 300 °C.

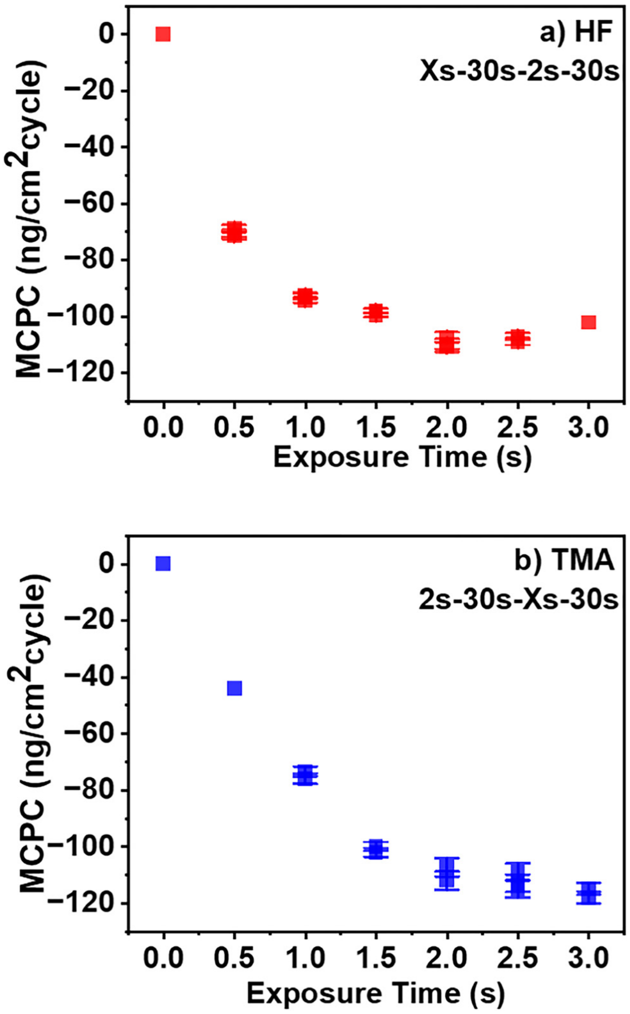

FIG. 7. MCPC at 275 °C vs precursor exposure time for (a) HF exposure with TMA exposure fixed at 2 s and (b) TMA exposure with HF exposure fixed at 2 s.

ALE was evaluated by varying the exposure time of one precursor while fixing the other precursor exposure time. The MCPC values and the error limits were determined at each exposure time over multiple ALE cycles. In Fig. 7(a), the MCPC decreases and then stabilizes at −109 ng/(cm^2 cycle) as the exposure time of HF increases with the TMA exposure time fixed at 2 s. This leveling off of the MCPC indicates a self-limiting behavior for the HF fluorination reaction. This result indicates that the 2 s exposure time of HF is sufficient to saturate the fluorination reaction.

The observed self-limiting behavior is attributed to the formation of a surface fluoride layer during the HF exposure. This passivating fluoride layer acts as a diffusion barrier and makes subsequent fluorination more difficult. Such diffusion-barrier-controlled surface modification has previously been described by the Deal–Grove model,[47] originally developed for Si oxidation and later extended to other metal oxidation systems. Comparable effects have also been reported for HF fluorination of Al_2O_3.[48]

Figure 7(b) analyzes the self-limiting behavior of the TMA ligand-exchange/conversion reaction. The MCPC shows self-limiting behavior when the exposure time of HF was kept at 2 s and the TMA exposure time was gradually increased from 0 to 3 s. This behavior is attributed to the finite fluoride layer thickness. After the fluoride layer has been removed, the ligand-exchange reaction can no longer occur. However, the TMA can proceed and convert some SnO_2 to Al_2O_3. This conversion will then influence the subsequent fluorination reaction. The conversion of SnO_2 to Al_2O_3 probably explains some of the initiation behavior observed in Fig. 6.

Figure 8 presents the QCM mass evolution for SnO_2 ALE conducted at 225, 250, 275, and 300 °C with the HF and TMA sequence of 2 s–30 s–2 s–30 s. Very linear removal of the SnO_2 mass was observed versus the number of ALE cycles at all temperatures. The SnO_2 ALE rate increases from 0.47 Å/cycle at 225 °C to 0.64 Å/cycle at 250 °C. The etch rate then rises more sharply to 1.44 Å/cycle at 275 °C and reaches 1.78 Å/cycle at 300 °C. These etch rates are all based on the SnO_2 density of 6.95 g/cm^3. The larger etch rate increase observed when the temperature increases from 250 to 275 °C could result from more effective conversion of SnO_2 to Al_2O_3 at higher temperature.

The magnitude of the mass change during each cycle of SnO_2 ALE depends on temperature. Figure 9 shows two representative ALE cycles at temperatures of 225, 250, 275, and 300 °C. These ALE cycles

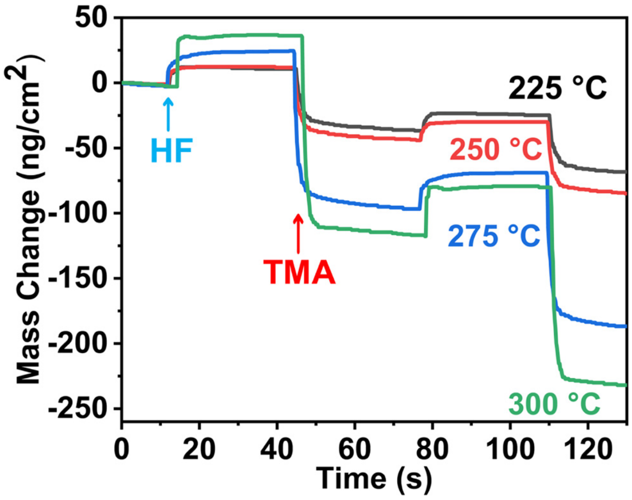

FIG. 9. Expansion of two ALE cycles in Fig. 8 showing the individual mass changes during the sequential HF and TMA exposures at 225, 250, 275, and 300 °C.

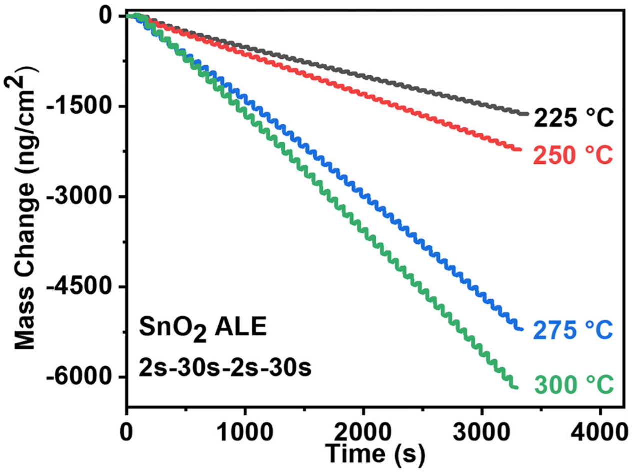

FIG. 8. Mass change vs time for SnO_2 ALE using sequential HF and TMA exposures at 225, 250, 275, and 300 °C with 2 s–30 s–2 s–30 s reaction sequence.

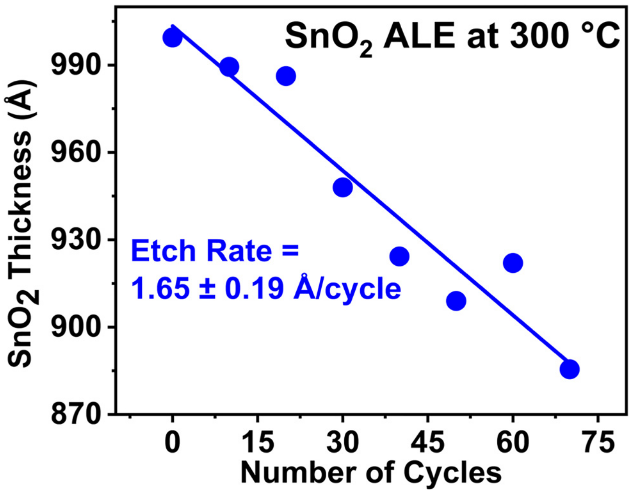

FIG. 10. Thickness change of the SnO_2 film vs number of thermal ALE cycles at 300 °C determined by XRR measurements.

are taken from the QCM results shown in Fig. 8. The results indicate that the fluorination occurring during the HF reaction and the mass loss during the TMA ligand-exchange/conversion reaction both increase with temperature. The fluorination and ligand-exchange/conversion reactions could both be temperature-dependent.

D. XRR and AFM measurements

The SnO_2 etch rate was also determined by XRR measurements. The SnO_2 films were deposited by SnO_2 ALD on Si(100) substrates at 300 °C. Figure 10 plots the thickness change of SnO_2 ALD films etched at 300 °C versus ALE cycle number. Each point on the graph corresponds to a fresh SnO_2 ALD film that was etched for the given number of ALE cycles. These measurements yield an SnO_2 ALE etch rate of 1.65 ± 0.19 Å/cycle at 300 °C. Despite some scatter among individual SnO_2 ALD films, the etch rate from XRR measurements is consistent with the 1.78 Å/cycle value measured by QCM experiments.

Figure 11(a) shows an AFM image with dimensions of $5 \times 5\,\mu m^2$ of an initial SnO_2 ALD film deposited at 300 °C. This

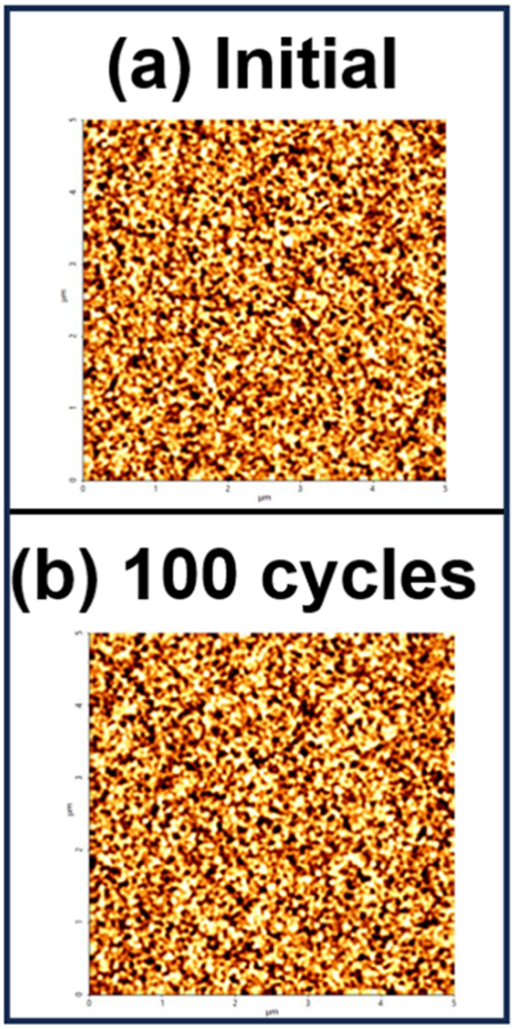

FIG. 11. AFM images of the (a) initial SnO_2 ALD film and (b) SnO_2 film after 100 ALE cycles at 300 °C. Dimensions of these AFM images are $5 \times 5\,\mu m^2$.

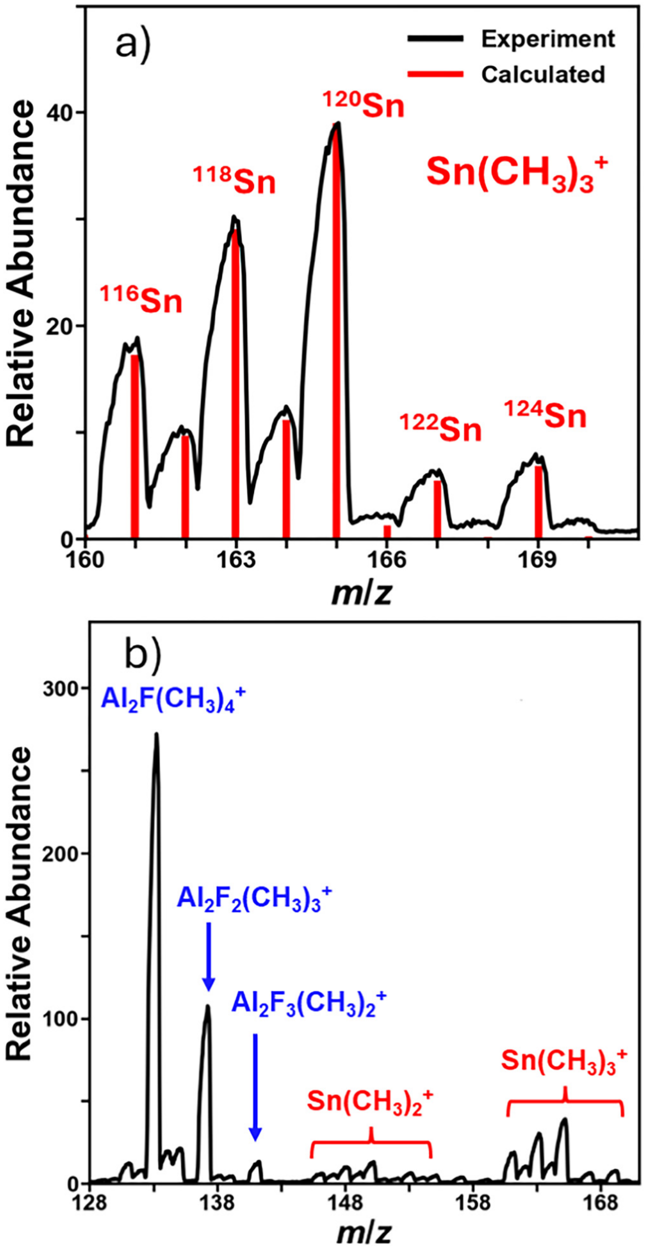

FIG. 12. Mass spectra recorded during TMA exposure on fluorinated SnO_2 powder at 300 °C. (a) Mass spectrum from m/z 160 to 170 showing ion signal intensities for $Sn(CH_3)_3^+$. (b) Mass spectrum from m/z 128 to 170 showing signal intensities for both $Sn(CH_3)_3^+$ and $Al_2F_x(CH_3)_y^+$ ion species.

film has an RMS roughness of 2.07 nm. Figure 11(b) displays a very similar AFM image with dimensions of $5 \times 5\,\mu m^2$ of the same SnO_2 ALD film after 100 thermal ALE cycles at 300 °C. This SnO_2 film has a RMS roughness of 2.14 nm. These surface roughness characterizations from AFM analysis and others after 30 and 70 ALE cycles indicate that the SnO_2 surface roughness is not changed by SnO_2 thermal ALE.

E. QMS studies of volatile etch products

QMS was used to identify the volatile etch products during the etching of SnO_2 by HF and TMA. To clarify the SnO_2 mechanism, sequential HF and TMA exposures were applied to SnO_2 powder at 300 °C. Figure 12(a) shows the QMS results for m/z values from 160 to 170 amu during TMA exposure on fluorinated SnO_2 powder at 300 °C during the first HF/TMA cycle. The ion intensities at different m/z values are consistent with these ion signals being derived from $Sn(CH_3)_3^+$. The $Sn(CH_3)_3^+$ ion signal is the main mass fragment from the ionization of the $Sn(CH_3)_4$ parent.[47]

$Sn(CH_3)_4$ is the expected Sn-containing etch product from the ligand-exchange and conversion reactions as shown in Fig. 1. Figure 12(a) also compares the experimental ion signal intensities and the calculated peak intensities expected from the natural abundances of the Sn and C isotopes. The seven main isotopes of Sn are ^{116}Sn at 14.5%, ^{117}Sn at 7.7%, ^{118}Sn at 24.3%, ^{119}Sn at 8.6%, ^{120}Sn at 32.6%, ^{122}Sn at 4.6%, and ^{124}Sn at 5.8%. The largest ion intensity is observed at m/z 165 corresponding to $^{120}Sn(CH_3)_3^+$. The next largest ion intensity is measured at m/z 163 corresponding to $^{118}Sn(CH_3)_3^+$. The other peaks can all be explained based on the other Sn and C isotopes. Their experimental intensities are in excellent agreement with the peak intensities expected from the natural isotopic abundances.

Ligand-exchange products derived from $AlF(CH_3)_2$ [dimethylaluminum fluoride (DMAF)] are also expected from the TMA ligand-exchange reaction displayed in Fig. 1. As observed during earlier QMS studies on Al_2O_3 thermal ALE using sequential HF and TMA exposures, the DMAF etch products undergo dimerization with either themselves or TMA.[45,48] These Al dimers were also predicted as the stable ligand-exchange products by theoretical calculations.[49,50] The Al dimer species are observed in Fig. 12(b) during SnO thermal ALE. $Al_2F(CH_3)_4^+$, $Al_2F_2(CH_3)_3^+$, and $Al_2F_3(CH_3)_2^+$ ion signals are observed at m/z 133, 137, and 141. The previous QMS studies during Al_2O_3 thermal ALE also measured the prominent Al dimer species at m/z 133 and 137.[45,48] In addition, Fig. 12(b) also shows the $Sn(CH_3)_3^+$ and $Sn(CH_3)_2^+$ ion signals around m/z 165 and 150, respectively. The ion signal for $Al_2F(CH_3)_4^+$ at m/z 133 is approximately six times larger than the ion signal for $Sn(CH_3)_3^+$ at m/z 165.

Figure 13 shows the time-dependence of the QMS signals during HF and TMA exposures on SnO_2 powder at 300 °C. Figure 13(a) clearly observes the production of H_2O at the onset of the HF exposure on the SnO_2 powder. As illustrated in Fig. 1 and given by Eq. (2), H_2O is produced by the HF fluorination reaction. The absence of the HF^+ ion signal during the initial rise of the H_2O^+ ion signal is consistent with all the HF consumed at the beginning of the HF exposure. The HF reaction is also self-limiting because the H_2O yield decreases as the HF signal rises and reaches a fairly constant level in Fig. 13(a).

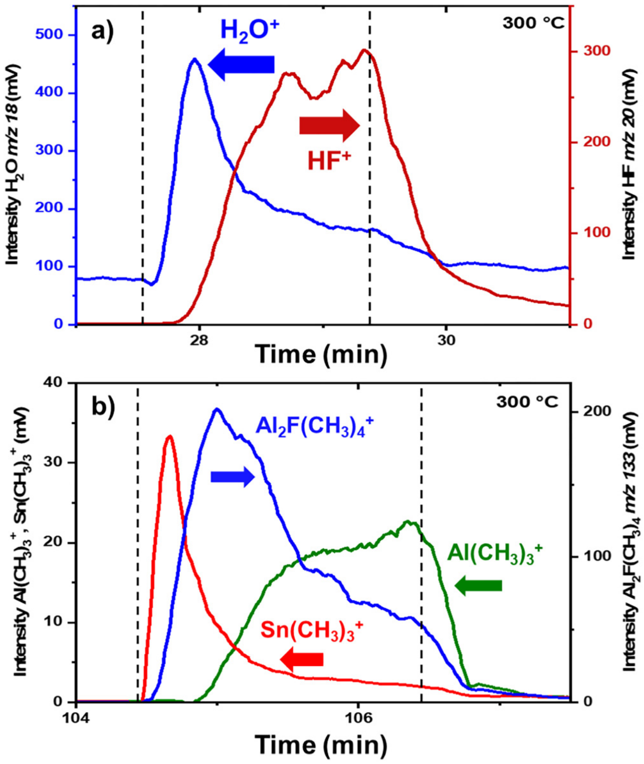

FIG. 13. Time-resolved QMS results during HF and TMA exposures at 300 °C. (a) H_2O^+ and HF^+ ion intensities during HF exposure. (b) $Sn(CH_3)_3^+$, $Al_2F(CH_3)_4^+$, and $Al(CH_3)_3^+$ ion intensities during TMA exposure.

The ion signals during the subsequent TMA exposure on the fluorinated SnO_2 sample are displayed in Fig. 13(b). The $Sn(CH_3)_3^+$ ion signal intensity appears immediately with the start of the TMA exposure. As mentioned earlier, $Sn(CH_3)_3^+$ is the main ion fragment from the electron impact ionization of $Sn(CH_3)_4$.[47] In agreement with Fig. 1 and Eq. (4), $Sn(CH_3)_4$ is the Sn product from the conversion reactions.

Figure 13(b) also shows that the $Al_2F(CH_3)_4^+$ ion intensity rises as the $Sn(CH_3)_3^+$ ion intensity decreases. The time delay in Fig. 13(b) for the appearance of the Al dimer signal relative to the $Sn(CH_3)_4$ signal indicates that the Al dimer reaction products derived from DMAF may initially be adsorbed to the fluorinated surface. The Al dimer reaction products may be bound to the surface by strong F-bridge bonding between the surface fluorides and Al.[51] This strong F-bridge bonding may allow the $Sn(CH_3)_4$ products to desorb first.

There is also a possibility that the HF may fluorinate both the converted Al_2O_3 layer and the underlying SnO_2. The TMA would then have the possibility to produce Al dimer reaction products from ligand-exchange with AlF_3 and $Sn(CH_3)_4$ from ligand-exchange with SnF_4. The $Sn(CH_3)_4$ may be more volatile and desorb first from the surface because there is no F-bridge bonding. The desorption of the Al dimers may also require lower surface fluorine coverages resulting from the progressive ligand-exchange reactions with TMA. In addition, higher coverages of TMA and DMAF may be required to desorb the Al dimers.

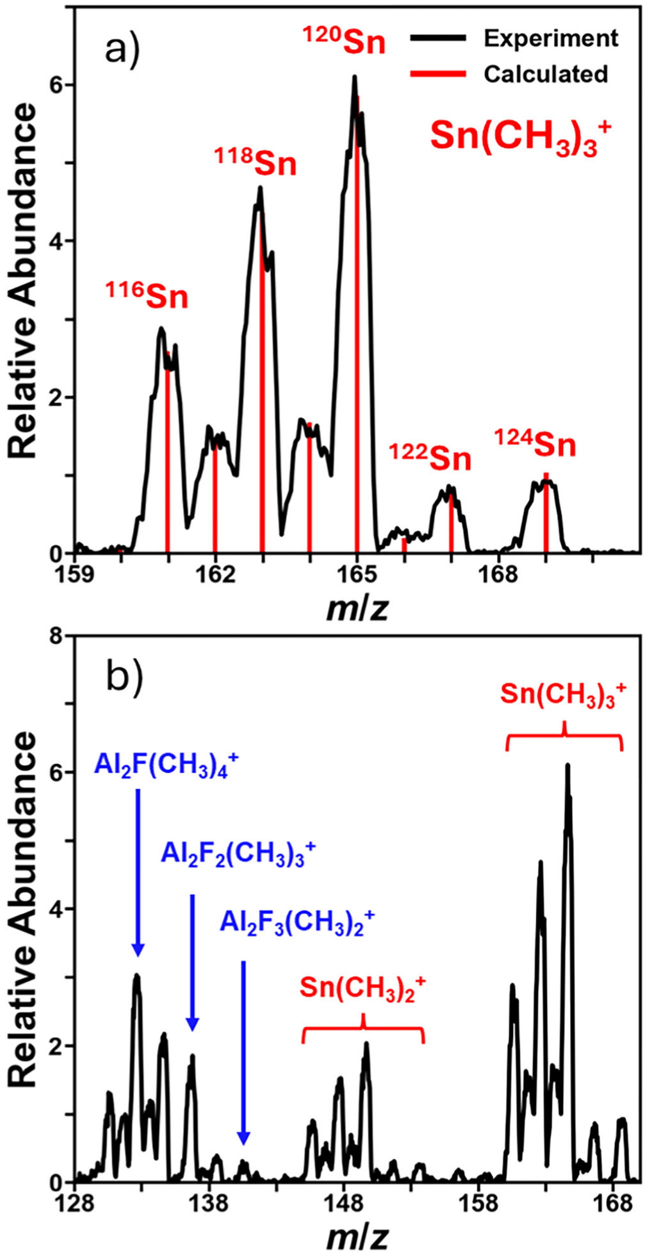

FIG. 14. Mass spectra recorded during TMA exposure on initial fresh SnO_2 powder prior to HF exposure at 300 °C. (a) Mass spectrum from m/z 159 to 171 showing ion signal intensities for $Sn(CH_3)_3^+$. (b) Mass spectrum from m/z 128 to 169 showing signal intensities for both $Sn(CH_3)_3^+$ and $Al_2F_x(CH_3)_y^+$ ion species.

Figure 13(b) also reveals that the $Al(CH_3)_3^+$ ion signal increases as the $Al_2F(CH_3)_4^+$ ion intensity decreases. The $Al_2F(CH_3)_4^+$ ion intensity continues to decrease during the TMA exposure. This self-limiting behavior suggests that the TMA exposure eventually depletes the surface fluorine coverage. However, the $Sn(CH_3)_3^+$ and $Al_2F(CH_3)_4^+$ ion intensities persist until the end of the TMA exposure. The continual presence of the $Sn(CH_3)_3^+$ and $Al_2F(CH_3)_4^+$ ion intensities during the TMA exposure in Fig. 13(b) provides evidence for the conversion of SnO_2 to Al_2O_3 by TMA after the ligand-exchange reaction.

To test for the conversion of SnO_2 to Al_2O_3 without the complication of the ligand-exchange reaction, experiments were conducted for TMA exposures on SnO_2 powder prior to any HF exposures. Figure 14 shows the QMS results during TMA exposure on fresh, initial SnO_2 ALD films at 300 °C. The QMS measurements in Fig. 14(a) reveal the presence of $Sn(CH_3)_3^+$ ion intensities from the first TMA exposure on SnO_2 before any HF exposure. The $Sn(CH_3)_4$ product is consistent with the reaction given in Eq. (4). This conversion reaction is thermochemically favorable. Thermochemical calculations reveal that the standard Gibbs free energy change for Eq. (4) is $\Delta G°$ (300 °C) = −292.9 kcal.[46] This large negative $\Delta G°$ is consistent with a spontaneous reaction.

The detection of $Sn(CH_3)_4$ during TMA exposure to fresh SnO_2 powder indicates that $Sn(CH_3)_4$ can be derived from either the ligand-exchange reaction between TMA and SnF_4 or the conversion of SnO_2 to Al_2O_3 by TMA. During SnO_2 ALE, TMA could produce $Sn(CH_3)_4$ by ligand-exchange with SnF_4. After removing the AlF_3 and SnF_4 surface fluorides, the TMA can proceed to produce $Sn(CH_3)_4$ when the underlying SnO_2 surface is converted to Al_2O_3.

The mass spectrum in Fig. 14(b) also shows the presence of Al dimer species during the TMA exposures on fresh SnO_2 powder. The Al dimer species in Fig. 14(b) are believed to result from TMA ligand-exchange reactions on the fluorinated gas line that delivers HF and TMA reactants to the powder sample. These ligand-exchange reactions could also form Al dimer species that flow through the powder sample and are detected by the mass spectrometer. The ion signal for $Sn(CH_3)_3^+$ at m/z 165 in Fig. 14(b) is approximately two times larger than the ion signal for $Al_2F(CH_3)_4^+$ at m/z 133. A comparison between Figs. 12(b) and 14(b) also reveals that much more $Sn(CH_3)_3^+$ ion intensity relative to $Al_2F(CH_3)_4^+$ ion intensity is observed for TMA exposures on fresh SnO_2 powders.

IV. CONCLUSIONS

Sequential, self-limiting fluorination and ligand-exchange/conversion reactions were demonstrated for SnO_2 thermal ALE using HF and TMA. During this two-step ALE process, TMA can convert SnO_2 to Al_2O_3. HF then fluorinates the Al_2O_3 metal oxide to form metal fluoride. TMA can then volatilize the metal fluoride by a ligand-exchange reaction before continuing to convert more SnO_2 to Al_2O_3.

Using SnO_2 films grown using SnO_2 ALD, *in situ* QCM experiments monitored SnO_2 ALE over a range of temperatures from 225 to 300 °C. The SnO_2 etching rates increased at higher temperatures. The MCPC values were −32.6, −44.2, −100.2, and −123.5 ng/(cm^2 cycle) at 225, 250, 275, and 300 °C, respectively.

These MCPCs correspond to SnO_2 etch rates of 0.47, 0.64, 1.44, and 1.78 Å/cycle for 225, 250, 275, and 300 °C, respectively.

The QCM measurements revealed that the mass of the SnO_2 films decreased linearly with the number of SnO_2 ALE cycles. QCM analysis also determined that the HF and TMA reactions were self-limiting. XRR investigations monitored the linear removal of the SnO_2 film thickness versus the number of ALE cycles and obtained etch rates that were consistent with the QCM measurements. AFM studies revealed that the roughness of the SnO_2 surface did not change versus the number of ALE cycles.

The volatile etch products during the sequential HF and TMA exposures on SnO_2 at 300 °C were determined by QMS analysis. $Sn(CH_3)_4$ was identified as the main Sn etch product during TMA exposures. This $Sn(CH_3)_4$ etch product results from the ligand-exchange and conversion reactions. Additional ligand-exchange etch products include $Al_xF_y(CH_3)_z$ dimer and trimer species resulting from the DMAF monomer together with itself and TMA.

The QMS studies also determined that $Al(CH_3)_3$ exposures on fresh, initial SnO_2 substrates prior to any fluorination released $Sn(CH_3)_4$ products. These $Sn(CH_3)_4$ products result from a conversion reaction when TMA converts SnO_2 to Al_2O_3. The time-resolved QMS results during TMA exposures during SnO_2 ALE also indicated that TMA can convert SnO_2 to Al_2O_3 after the TMA ligand-exchange reactions with the fluorinated surface.

ACKNOWLEDGMENTS

This research was funded by the SEMES Etch Team. Additional support was provided by the Center for Heterogeneous Integration of Micro Electronic Systems (CHIMES), one of the seven centers sponsored by the Semiconductor Research Corporation (SRC) and DARPA under the Joint University Microelectronics Program 2.0 (JUMP 2.0). Funding for the QMS reactor and the QMS investigations was provided by Lam Research. The authors also thank Rebecca Hirsch for the XRD and XRR measurements.

AUTHOR DECLARATIONS

Conflict of Interest

The authors have no conflicts to disclose.

Author Contributions

Chen Li: Data curation (lead); Formal analysis (lead); Investigation (lead); Writing – original draft (lead); Writing – review & editing (supporting). **Jonathan L. Partridge:** Data curation (equal). **Troy A. Colleran:** Data curation (equal). **Micah H. Duffield:** Data curation (equal). **Yong Hyun Ham:** Conceptualization (equal); Funding acquisition (equal). **Steven M. George:** Conceptualization (equal); Formal analysis (supporting); Funding acquisition (equal); Methodology (lead); Project administration (lead); Supervision (lead); Writing – original draft (supporting); Writing – review & editing (lead).

DATA AVAILABILITY

The data that support the findings of this study are available within the article.

REFERENCES

[1] K. Ellmer, Nat. Photonics **6**, 809 (2012).

[2] M. Grundmann, H. Frenzel, A. Lajn, M. Lorenz, F. Schein, and H. von Wenckstern, Phys. Status Solidi A **207**, 1437 (2010).

[3] M. Batzill and U. Diebold, Prog. Surf. Sci. **79**, 47 (2005).

[4] Z. Galazka *et al.*, Phys. Status Solidi A **211**, 66 (2014).

[5] G. K. Dalapati *et al.*, J. Mater. Chem. A **9**, 16621 (2021).

[6] A. Sharma, A. Ahmed, A. Singh, S. K. Oruganti, A. Khosla, and S. Arya, J. Electrochem. Soc. **168**, 027505 (2021).

[7] D. D. Liang, B. J. Chen, B. Feng, Y. Ikuhara, H. J. Cho, and H. Ohta, ACS Appl. Nano Mater. **3**, 12427 (2020).

[8] C. Park, S. Kim, D. W. Lee, and R. B. K. Chung, Mater. Today Commun. **37**, 107064 (2023).

[9] D. P. Gao *et al.*, Science **386**, 187 (2024).

[10] A. Lan, H. Lu, B. Huang, F. Chen, Z. Chen, J. Wang, L. Li, and H. Do, ACS Appl. Mater. Interfaces **16**, 64825 (2024).

[11] X. Du and S. M. George, Sens. Actuators B **135**, 152 (2008).

[12] Y. Masuda, Sens. Actuators B **364**, 131876 (2022).

[13] V. K. Gueorguiev, L. I. Popova, G. D. Beshkov, and N. A. Tomajova, Sens. Actuators A **24**, 61 (1990).

[14] B. R. Wu, S. L. Ou, S. Y. Lo, H. Y. Mao, J. Y. Yang, and D. S. Wuu, J. Nanomater. **2014**, 907610 (2014).

[15] S. F. Chini and A. Amirfazli, Langmuir **26**, 13707 (2010).

[16] K. H. Kwon, A. Efremov, M. Kim, N. K. Min, J. Jeong, M. Hong, and K. Kim, J. Vac. Sci. Technol. A **28**, 226 (2010).

[17] J. C. Park, J. K. Kim, T. G. Kim, D. W. Lee, H. Cho, H. S. Kim, S. J. Yoon, and Y. G. Jung, Int. J. Mod. Phys. B **25**, 4237 (2011).

[18] R. Edel, E. Alexander, T. Nam, A. S. Cavanagh, T. Van Voorhis, and S. M. George, J. Vac. Sci. Technol. A **42**, 062602 (2024).

[19] A. Fischer, A. Routzahn, S. M. George, and T. Lill, J. Vac. Sci. Technol. A **39**, 030801 (2021).

[20] S. M. George, Acc. Chem. Res. **53**, 1151 (2020).

[21] T. Faraz, F. Roozeboom, H. C. M. Knoops, and W. M. M. Kessels, ECS J. Solid State Sci. Technol. **4**, N5023 (2015).

[22] Y. Lee and S. M. George, J. Phys. Chem. C **123**, 18455 (2019).

[23] H. Ohtake, N. Miyoshi, K. Shinoda, S. Fujisaki, and Y. Yamaguchi, Jpn. J. Appl. Phys. **62**, Sg0801 (2023).

[24] S. M. George and Y. Lee, ACS Nano **10**, 4889 (2016).

[25] A. M. Cano, A. Lii-Rosales, and S. M. George, J. Phys. Chem. C **126**, 6990 (2022).

[26] N. R. Johnson, J. K. Hite, M. A. Mastro, C. R. Eddy, and S. M. George, Appl. Phys. Lett. **114**, 243103 (2019).

[27] Y. Lee, J. W. DuMont, and S. M. George, Chem. Mater. **28**, 2994 (2016).

[28] Y. Lee and S. M. George, ACS Nano **9**, 2061 (2015).

[29] Y. Lee and S. M. George, J. Vac. Sci. Technol. A **36**, 061504 (2018).

[30] Y. Lee, N. R. Johnson, and S. M. George, Chem. Mater. **32**, 5937 (2020).

[31] J. Reif, M. Knaut, S. Killge, M. Albert, T. Mikolajick, and J. W. Bartha, J. Vac. Sci. Technol. A **40**, 032602 (2022).

[32] J. W. DuMont, A. E. Marquardt, A. M. Cano, and S. M. George, ACS Appl. Mater. Interfaces **9**, 10296 (2017).

[33] D. R. Zywotko and S. M. George, Chem. Mater. **29**, 1183 (2017).

[34] J. C. Gertsch, J. L. Partridge, A. M. Cano, J. W. Clancey, V. M. Bright, and S. M. George, J. Vac. Sci. Technol. A **41**, 012603 (2023).

[35] A. M. Cano, J. L. Partridge, and S. M. George, Chem. Mater. **34**, 6440 (2022).

[36] A. I. Abdulagatov and S. M. George, J. Vac. Sci. Technol. A **38**, 022607 (2020).

[37] A. I. Abdulagatov and S. M. George, Chem. Mater. **30**, 8465 (2018).

[38] A. I. Abdulagatov, V. Sharma, J. A. Murdzek, A. S. Cavanagh, and S. M. George, J. Vac. Sci. Technol. A **39**, 022602 (2021).

[39] E. Mohimi, X. I. Chu, B. B. Trinh, S. Babar, G. S. Girolami, and J. R. Abelson, ECS J. Solid State Sci. Technol. **7**, P491 (2018).

[40] J. A. Murdzek, A. Lii-Rosales, and S. M. George, Chem. Mater. **33**, 9174 (2021).

[41] J. A. Murdzek, A. Lii-Rosales, and S. M. George, J. Vac. Sci. Technol. A **41**, 032603 (2023).
[42] J. W. Elam, M. D. Groner, and S. M. George, Rev. Sci. Instrum. **73**, 2981 (2002).
[43] J. W. Elam, D. A. Baker, A. J. Hryn, A. B. F. Martinson, M. J. Pellin, and J. T. Hupp, J. Vac. Sci. Technol. A **26**, 244 (2008).
[44] J. L. Partridge, J. A. Murdzek, V. L. Johnson, A. S. Cavanagh, A. Fischer, T. Lill, S. Sharma, and S. M. George, Chem. Mater. **35**, 2058 (2023).
[45] A. Lii-Rosales, A. S. Cavanagh, A. Fischer, T. Lill, and S. M. George, Chem. Mater. **33**, 7719 (2021).
[46] HSC Chemistry 5, Outokumpu Research Oy, Pori, Finland.
[47] NIST Mass Spectrometry Data Center, William E. Wallace, director, "Mass spectra," in *NIST Chemistry WebBook, NIST Standard Reference Database Number 69*, edited by P. J. Linstrom and W. G. Mallard (National Institute of Standards and Technology, Gaithersburg, MD, 2025), p. 20899.
[48] J. W. Clancey, A. S. Cavanagh, J. E. T. Smith, S. Sharma, and S. M. George, J. Phys. Chem. C **124**, 287 (2020).
[49] X. Hu and J. Schuster, J. Phys. Chem. C **126**, 7410 (2022).
[50] K. Khumaini, G. Cho, H. L. Kim, and W. J. Lee, Surf. Interfaces **72**, 107114 (2025).
[51] H. W. Roesky and I. Haiduc, J. Chem. Soc. Dalton Trans. **14**, 2249 (1999).